

# Check your Air Data - Setup and Practical Examples for the Flight Data Compatibility Check

**Christian Raab**

Research Scientist, DLR (German Aerospace Center), Institute of Flight Systems, 38108, Braunschweig, Germany. [christian.raab@dlr.de](mailto:christian.raab@dlr.de)

## ABSTRACT

Accurate information about aircraft speed, altitude, and aerodynamic flow angles is essential for evaluating aircraft performance and handling qualities. These quantities are determined from air data measurements taken by sensors normally located near the aircraft cockpit. Since these sensors are affected by the distorted flow field around the fuselage, a correction must be applied. Before the first flight, a set of calibration parameters is usually determined from wind tunnel experiments or CFD calculations. However, the Data Compatibility Check (DCC) method allows a more accurate air data sensor calibration during the certification flight test. This method reconstructs air data quantities from inertial acceleration, angular rate measurements and the flight path. By comparing the reconstructed quantities with the measured ones, the structure and parameters of air data sensor models can be identified. In this paper an introduction to the data compatibility check method and the setup used in a flight test for system identification is given. The DCC is applied on data gathered from a test campaign with the new DLR research aircraft Dassault Falcon 2000LX ISTAR. Use cases for the calibration of the nose boom airflow vanes and the correction of sensors during large sideslip maneuvers will be presented in this paper.

**Keywords:** Flight Test, Data Compatibility Check, Flight Path Reconstruction, Sensor Measurements, Air Data

## Nomenclature

$\alpha, \beta$	=	angle of attack, angle of sideslip, rad
$a_n$	=	sonic speed at Mean Sea Level (MSL) (340.294 m/s)
$a_x, a_y, a_z$	=	translational acceleration along the body axis, m/s <sup>2</sup>
$b$	=	bias parameter.
$\gamma_H$	=	International Standard Atmosphere (ISA) temperature gradient (-0.0065 K/m, tropopause)
$g_0$	=	normal earth acceleration (9.80665 m/s <sup>2</sup> )
$f$	=	factor parameter
$Ma$	=	Mach number
$p_n$	=	standard atmosphere pressure at MSL (101325 Pa)
$p_{stat}$	=	static pressure, Pa
$p_{tot}$	=	total pressure, Pa
$p, q, r$	=	roll, pitch and yaw rate, rad/s
$\Phi, \Theta, \Psi$	=	roll, pitch and yaw angle, rad
$\sigma_s$	=	standard deviation
$T_N$	=	standard atmosphere static air temperature at MSL (288.15 K)
$T_{tot}$	=	total air temperature, K
$T_{stat}$	=	static air temperature, K
$h$	=	altitude, m
$h_{baro}$	=	barometric Altitude, m

$\kappa$	=	isentropic exponent for air (1.4)
$R$	=	specific gas constant of dry air (287.05287 J/kgK)
$t$	=	time, s
$\tau$	=	time delay, s
$V_N, V_E, V_D$	=	inertial velocities in north, east and downward geodetic direction, m/s
$V_{TAS}$	=	true airspeed, m/s
$V_{CAS}$	=	computed airspeed, m/s
$x, y, z$	=	position coordinates, m

### Subscripts

$A$	=	aerodynamic velocity
$ADS$	=	air data system
$AOA, AOS$	=	angle of attack, angle of sideslip
$avg$	=	averaged value
$b$	=	body-fixed frame
$CG$	=	center of gravity
$g$	=	geodetic frame
$IRS$	=	inertial reference system
$K$	=	inertial velocity
$LH, RH$	=	left hand, right hand
$l$	=	local reconstructed value
$m$	=	model output
$s$	=	sensor output, measured signal
$NB$	=	nose boom
$W$	=	wind velocity

## 1 Introduction

### 1.1 The Importance of Accurate Flight Data

Evaluating the performance, control, and stability characteristics of the aircraft is the primary objective of a certification flight test program. For this reason, a large number of parameters are measured and recorded during the flight test. Before these raw measurements can be analyzed and used for other applications, they must be checked for errors and consistency. The determination of systematic instrument errors such as scale factors, zero shifts and time delays is the scope of the Data Compatibility Check (DCC) method described in this paper. It relies on the kinematic relationship between inertial and air data measurements. For example, the measured angle of attack must match the one reconstructed from the measured inertial accelerations and angular rates in order to verify compatibility. The comparison between the measured and the reconstructed quantities can be used in an optimization process for the identification of sensor models. This data processing step is referred to as Flight Path Reconstruction (FPR) and aims to derive calibration functions from the identified sensor models that could be used to correct the measured air and inertial data. The corrected flight test signals are used for several purposes e.g.:

- Calibration of the standard air data system during certification flight tests,
- system identification of an aerodynamic model that is used in the development of flight control applications and training devices,
- comparisons with Computational Fluid Dynamics (CFD) calculations, where accurate determination of aerodynamic flow quantities such as Mach number and angle of attack are important,
- selection and characterization of input signals for flight control augmentation systems.

Very often, redundant signals from different sensor systems are included in the set of recorded flight parameters. In this case, the DCC results support the selection of the flight parameter with the best measurement quality. There are two main approaches to the FPR process that can be found in the literature. The first one is a stochastic approach based on the extended Kalman filter [1, 2]. In this case, sensor model parameters and aircraft states are

estimated simultaneously. These filtering methods can be used in an online application and can account for noise in the input and output variables. However, they require good a-priori knowledge of the sensor noise characteristics. The second approach is deterministic, where the aircraft states are determined from the equations of motion and sensor models are developed. For the estimation of sensor parameters and initial states, the model output is compared to sensor measurements using a Maximum Likelihood algorithm [3]. This method is more flexible than the filtering technique and can be combined with the subsequent task of aerodynamic system identification. It has been successfully applied in several system identification projects at DLR [4].

It should be noted that other methods for calibrating air data sensors exist in the Flight Test community. In reference [5], measurements taken at stationary horizontal level flight conditions, trimmed at different speeds and altitudes, are used to calibrate the  $\alpha$  measurements of a nose boom. Static air pressure sensors usually are calibrated using trailing cone flights and tower flyby methods as presented in reference [6]. The DCC cannot replace a basic calibration of reference instruments like static pressure and nose boom sensors. However, in combination with a good reference instrumentation it leads to a better overall quality of the measured flight data and also accounts for dynamic motion effects. As the DCC method can be applied continuously in parallel to the flight test program, sensor errors can be identified quickly and corrections can be made on the fly. That way the time for flight data analysis during a certification test program can be optimized.

The following section present the DLR research aircraft and the evaluated sensors. Section 2 gives an overview of the flight test campaign for system identification and the flown maneuvers. The FPR process, the kinematic equations and the setup used for the ISTAR flight test campaign are described in section 3. Selected results of the applied DCC are presented in section 4, starting with a verification and correction of the nose-boom wind vane measurements, followed by the identified characteristics of the basic avionic angle of attack sensor. The shadowing effects of the static and total pressure sensors during large sideslip maneuvers are discussed in the last example. Finally, a conclusion and outlook on future flight test activities is given in section 5.

## 1.2 The DLR Research Aircraft ISTAR

The DLR research aircraft ISTAR (In-Flight Systems and Technologies Airborne Research) is a modified Dassault Falcon 2000LX as shown in Fig. 1. It has a wingspan of 21.38 m and an MTOW of 19.4 t. After delivery to DLR in 2020, the aircraft will be progressively equipped with an Experimental Flight Control System allowing direct access to the primary and secondary flight control surfaces [7]. This modification allows ISTAR to be used as a Variable Stability System for research on new guidance, navigation and control systems. These algorithms have to be designed and tested thoroughly on the ground before flight testing. An accurate flight dynamics model of the aircraft is required for this purpose. This model is used for hardware-in-the-loop testing and for flight preparation in a ground simulator of the ISTAR aircraft. In addition to the flight crew, the aircraft has space for five passengers, including a station for the flight test engineer and a station for data acquisition.



**Fig. 1 The DLR research aircraft ISTAR with installed nose boom. Credit: Uwe Bethke.**

## 1.3 Aircraft Sensors

The standard avionic on the Falcon 2000LX aircraft consists of two independent Air Data Systems (ADS) that measure and calculate information about atmospheric parameters [8]. Figure 2 shows a side view of the ISTAR with the location of the standard avionic air data sensors. Each ADS has separate sensors on the left hand and

right hand sides of the fuselage to measure total pressure  $p_t$ , static pressure  $p_s$ , total air temperature  $T_t$  and angle of attack  $\alpha$ . While each ADS has a pitot probe for measuring total pressure, there are two static ports on the left hand and right hand sides of the fuselage. The static pressure ports from each side are connected by a pressure tube to compensate for pressure differences. The total air temperature probe is located under the cockpit on the right hand side and contains two independent temperature sensors for ADS1 and ADS2. The static and total pressure ports are connected to the Air Data Modules (ADM) by tubes, containing the pressure sensors. A Modular Avionic Unit (MAU) processes the measurements from the pressure and total air temperature sensors and calculates the following air data quantities: static air temperature  $T_s$ , Mach number  $Ma$ , computed airspeed  $V_{CAS}$ , true airspeed  $V_{TAS}$ , pressure altitude  $h_p$ , corrected barometric altitude  $h_{baro}$ , and barometric vertical speed  $\dot{h}_p$ .



**Fig. 2 Location of the ISTAR standard avionic air data sensors.**

In normal operation, the ADS1 system provides the air data information for the captain’s primary flight display and the ADS2 system provides the data for the first officer’s display. The ADS signals on the avionic bus have a rate of 20 Hz and the  $\alpha$ -vane signals have a bus rate of 80 Hz. A standby air data system, consisting of separate static pressure and total pressure sensors on both fuselage sides provides backup air data information. The backup system is not connected to the flight test data acquisition bus, so measurements from the standby air data sensors were not available for DCC analysis.

Three Inertial Reference Systems (IRS) located in an electronics bay near the entrance door provide inertial velocities, geodetic position, and aircraft attitude and heading. Each IRS consists of three accelerometers and gyro sensors that measure accelerations and angular rates along and around the aircraft’s rigid axes at a rate of 80 Hz. The IRS is connected to a GPS receiver system that provides initial position values during the platform start-up procedure. The IRS also computes a hybrid IRS/GPS position, which is more accurate than a position determination based on IRS measurements alone. The acceleration and angular rate measurements of the basic avionic IRS are low-pass filtered, resulting in a slight time delay in the sensor output. Evaluation of the acceleration signal showed that the cut-off frequency is around 10 Hz, which is higher than the aircraft rigid body modes. Since the characteristics of the basic avionic IRS were not known at the start of the flight test campaign, a fourth experimental IRS platform was installed on the ISTAR aircraft to provide unfiltered output from the acceleration and gyro rate sensors at a sampling rate of 100 Hz.

System identification of an aerodynamic model requires an accurate determination of the atmospheric flow conditions. In addition to static and total pressure measurements, the angle of attack and angle of sideslip must be determined with an accuracy of well below  $0.5^\circ$ . For this reason, a nose boom as presented in Fig. 3 with air data sensors was installed on the front of the aircraft for the system identification flight test campaign. It allows the measurement of atmospheric parameters in front of the aircraft, where the influence of the fuselage on the air flow is minimal.

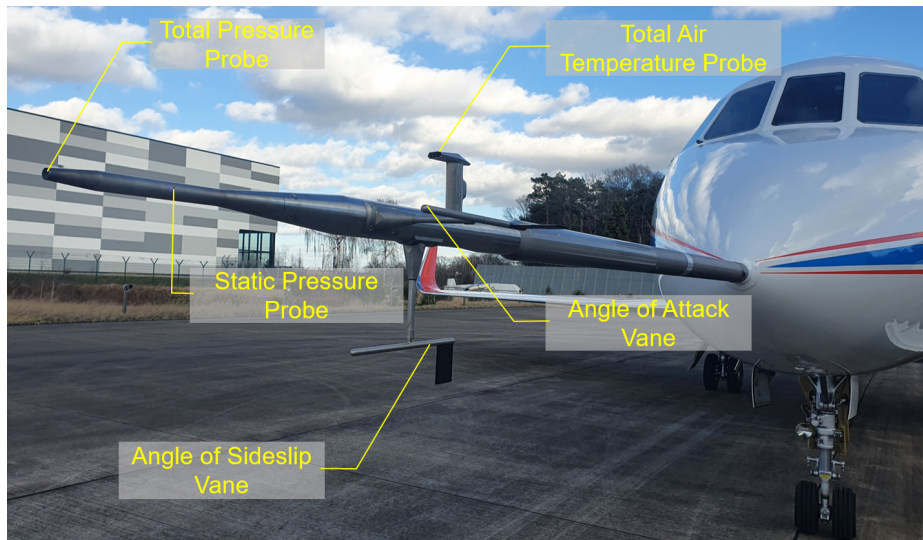


**Fig. 3** Nose boom installation with air data sensors.

Another important reason for installing the nose boom was the lack of sideslip information from the basic avionic sensors. The nose boom contains a total pressure probe at the tip of the boom and circularly placed cavities near the forward end to measure static pressure. A total air temperature sensor was installed at the top of the nose boom. All pressure sensors and the temperature probe have a sampling rate of 10 Hz. Wind vanes in the horizontal and vertical planes provide angle of attack and angle of sideslip information with a sampling rate of 20 Hz. After the installation of the nose boom and before the flight test, the output signals of the pressure sensors were calibrated on the ground by applying known air pressures. The angle of attack and angle of sideslip vane sensors were calibrated with a mechanical tool using a defined angle measurement scale. Offsets in the vane orientation to the aircraft body axes were also determined and used in the calibration equation. To calculate pressure measurements from the sensor Raw Binary Values (RBV), calibration equations were determined using a ground pressure calibration device. For all nose boom sensors Dassault Aviation provided a nose boom calibration for the measurement correction of each sensor. The calibration rules included look-up tables to correct the static pressure measurement. Due to the limited capacity of the on-board data acquisition computer, the correction, especially for the sideslip influence, had to be done in a post-processing step on the ground.

## 2 Flight Test

### 2.1 Test Points

The scope of the presented ISTAR system identification project is the development of a model representing the flight dynamics throughout the whole flight envelope. Test points were planned at different altitudes and speeds, taking into account different aircraft configurations, such as slat/flap settings and landing gear status. An overview of the flight envelope test points and the collected flight data is shown in Fig. 4. A total of 26 test points, including different flap and gear configurations, were completed with 9 test flights between February and May 2022. The red circles on the diagram represent the flight envelope test points, and the blue lines represent the flight data measurements collected during the flight test campaign. The flight envelope diagram shows system identification maneuvers, as well as level acceleration and deceleration flights, such as those performed at 30000 ft and tower fly-bys near the ground. Flight envelope test points no. 5, 6, 7 and 9 are not included in the current flight test data. The reason for this was extensive nose boom vibration that occurred at speeds near and above 300 kt  $V_{CAS}$ . This phenomenon of nose boom vibration is currently under investigation [9]. The aforementioned test items will be performed once the nose boom vibration issues have been resolved.

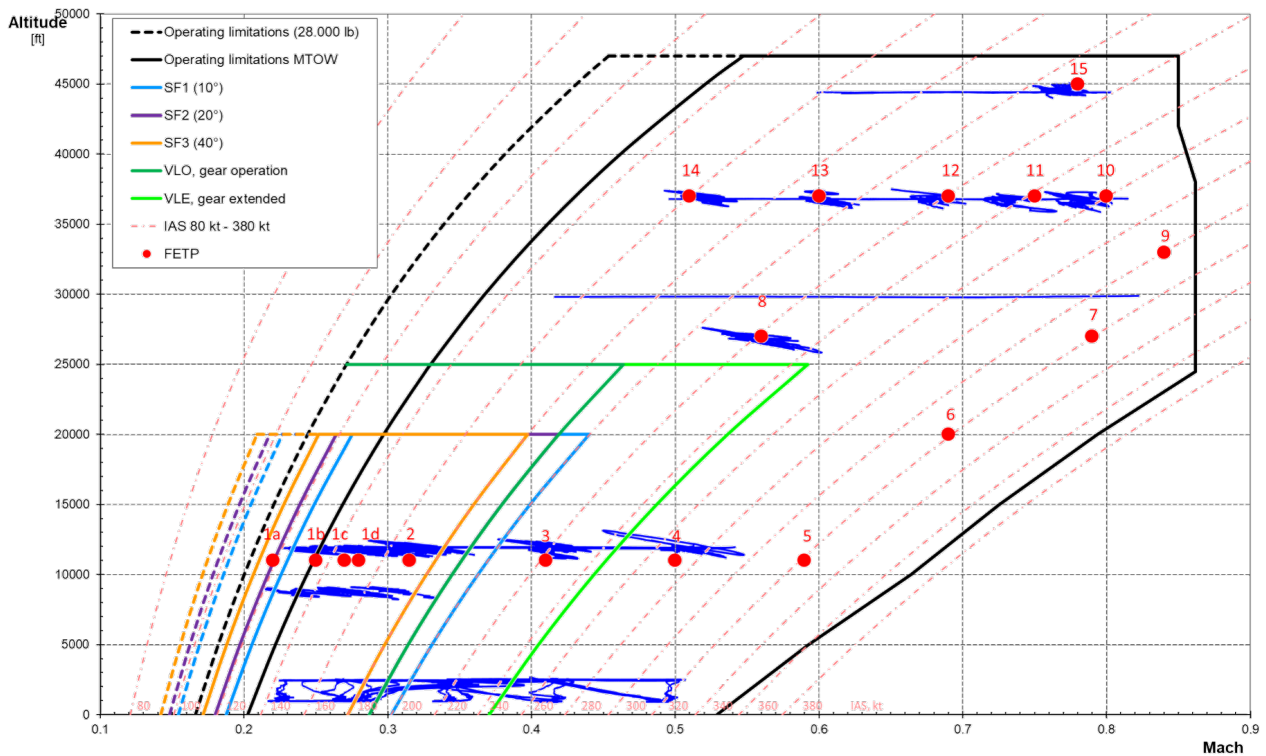


**Fig. 4 Overview of the flight data envelope with planned flight test points for system identification maneuvers (red circles) and the measured flight data (blue lines).**

## 2.2 Maneuvers and Collected Data

Independent excitation of the aircraft motion modes is the central objective of the system identification maneuvers. For the longitudinal motion, these excitation maneuvers included 1-3-2-1-1 step inputs on the elevator as well as small step inputs followed by a long free reaction time to observe the phugoid motion. Double step input excitations were also applied to the thrust lever and the horizontal stabilizer. To determine airbrake effectiveness, the airbrakes were deflected and retracted in a controlled manner. The lateral maneuvers included bank to bank turns, aileron and rudder doublets, and steady heading sideslip maneuvers. At some test points, combined maneuvers were performed such as a 1-3-2-1-1 elevator step input with a constant 30° bank angle.

Tower fly-bys were included in the flight test program to evaluate nose boom static pressure measurements. During these maneuvers, the aircraft was flown at an altitude of 150 - 200 ft above ground level near the tower in a level flight condition at a defined constant speed. The nose boom static pressure was compared to that measured with a calibrated pressure sensor on the airport tower.

Another part of the flight test program were acceleration and deceleration maneuvers at a constant defined altitude. In this case, only two test points were performed at 30000 ft and 45000 ft, because the maximum speed was limited to 300 kt  $V_{CAS}$  due to the nose boom vibrations. Flight data from these maneuvers will also be analyzed during the system identification process.

In total, over 590 maneuvers were performed during the flight test program, resulting in a total of 6.5 hours of recorded data. A good coverage of the angle of attack and angle of sideslip flight data is required for the aerodynamic system identification. An evaluation of the entire data set after the flight test program showed that the measurements covered an angle of attack range between -4° and 12° and a sideslip angle coverage between about -10° and 10°. The Mach number represented by the measured flight data ranged from 0.22 to 0.83. The results show that a good coverage of the operational envelope has already been obtained in the first flight test campaign. However, it should be noted that flight data at high angle of attack, near stall, are not currently part of the collected data. This will be part of the extended test program, collecting data near the envelope boundary at high and low speeds.

### 3 Method

The Data Compatibility Check is a higher-level process for checking and correcting flight test data. It is designed to ensure that data are consistent and that measurement errors are detected and corrected. One of the goals of the DCC is to develop sensor models that provide adequate agreement between the reference and measured airflow signals. In this step, the Flight Path Reconstruction (FPR) is applied to calculate reconstructed air data from inertial measurements. This process and the underlying equations are explained in the following sections.

#### 3.1 Flight Path Reconstruction Procedure

The Flight Path Reconstruction method is an essential part of the DCC which uses the measurements from the inertial reference system to determine the resulting aerodynamic flow quantities. These reconstructed signals can be compared to the measurements of the air data system. A schematic overview of the FPR procedure is depicted in Figure 5. The inertial accelerations and angular rates recorded during a flight maneuver are the input variables for the kinematic model of the aircraft motion.

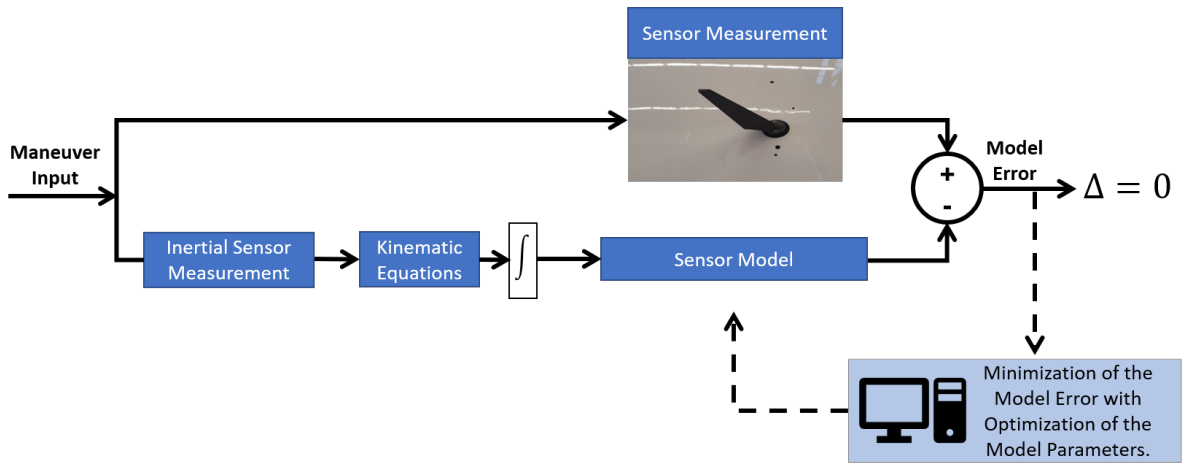


Fig. 5 Basic schematics of the FPR procedure.

Numerical integration of the kinematic equations yields the body-fixed airspeed components, which can be used to calculate angle of attack and angle of sideslip, and true airspeed  $V_{TAS}$ . The calculation of the kinematic equations and the associated aerodynamic flow quantities is explained in more detail in sections 3.2 and 3.3. Due to the assumed high reliability of the acceleration measurements, computed airflow signals are considered as reference and are compared with the measured ones. In an iterative process called the output error method, the model parameters are estimated with an optimization algorithm using Maximum Likelihood. A detailed description of the output error method and the FPR algorithm can be found in [4]. For each aircraft configuration (flap setting, landing gear status), a separate set of parameters was estimated, using all available flight test maneuvers for the considered configuration as input to the FPR procedure. The quality of the estimates was evaluated by the cost function obtained after each iteration and the standard deviation for each individual parameter. Weighted output signals, which are directly compared to the measured quantities and contribute to the calculation of the cost function, were defined. Details of this setup can be found in the section 3.4. The sensor model identification was performed with the DLR system identification software FITLAB [10].

#### 3.2 Kinematic Equations

The measured acceleration  $a_{xKb}^s, a_{yKb}^s, a_{zKb}^s$  and angular rates  $p_{Kb}^s, q_{Kb}^s, r_{Kb}^s$  are used to estimate the state variables using the kinematic relationship described in this section. The kinematic equations for the translational

accelerations in the body-fixed system are:

$$\dot{u}_{Kb} = a_{xKb}^s - q_{Kb}^s w_{Kb} + r_{Kb}^s v_{Kb} - g_0 \sin \Theta, \quad u(t_0)_{Kb} = u_0 \quad (1)$$

$$\dot{v}_{Kb} = a_{yKb}^s - r_{Kb}^s u_{Kb} + p_{Kb}^s w_{Kb} + g_0 \cos \Theta \sin \Phi, \quad v(t_0)_{Kb} = v_0 \quad (2)$$

$$\dot{w}_{Kb} = a_{zKb}^s - p_{Kb}^s v_{Kb} + q_{Kb}^s u_{Kb} + g_0 \cos \Theta \cos \Phi, \quad w(t_0)_{Kb} = w_0 \quad (3)$$

Transformation of the body-fixed velocities into the geodetic coordinate system results in the differential equations for the geodetic position which are:

$$\begin{aligned} \dot{x}_g = V_N &= u_{Kb} \cos \Theta \cos \Psi + v_{Kb} (\sin \Phi \sin \Theta \cos \Psi - \cos \Phi \sin \Psi) \\ &+ w_{Kb} (\cos \Phi \sin \Theta \cos \Psi + \sin \Phi \sin \Psi), \quad x_g(t_0) = x_{g,0} \end{aligned} \quad (4)$$

$$\begin{aligned} \dot{y}_g = V_E &= u_{Kb} \cos \Theta \sin \Psi + v_{Kb} (\sin \Phi \sin \Theta \sin \Psi + \cos \Phi \cos \Psi) \\ &+ w_{Kb} (\cos \Phi \sin \Theta \sin \Psi - \sin \Phi \cos \Psi), \quad y_g(t_0) = y_{g,0} \end{aligned} \quad (5)$$

$$\dot{h} = -V_D = u_{Kb} \sin \Theta - v_{Kb} \sin \Phi \cos \Theta - w_{Kb} \cos \Phi \cos \Theta, \quad h_g(t_0) = h_{g,0} \quad (6)$$

The body-fixed inertial velocity components  $u_{Kb}, v_{Kb}, w_{Kb}$  are determined by numerical integration of Eqs. 1 to 3. During the flight test, the maneuvers were performed in a calm atmosphere with no turbulence or gusts. Most of the maneuver time slices are of short duration, less than 30 seconds. Under these conditions, the horizontal wind was assumed to be constant and the vertical wind was assumed to be close to zero ( $w_{Wb} = 0$ ). With these assumptions, the horizontal wind components ( $u_{Wb}, v_{Wb}$ ) can be estimated during the FPR process by weighting the geodetic positions and inertial velocities at the model output. The aerodynamic velocity components were determined using the following equations:

$$u_{Ab} = u_{Kb} - u_{Wb} \quad (7)$$

$$v_{Ab} = v_{Kb} - v_{Wb} \quad (8)$$

$$w_{Ab} = w_{Kb} \quad (9)$$

In this way the aerodynamic velocities are reconstructed from the acceleration and angular rate measurements from the inertial reference platform. The aircraft attitude angles are determined by integrating the differential equation of the angular motion components, being defined by the following equations:

$$\dot{\Phi} = p_{Kb}^s + \tan \Theta (q_{Kb}^s \sin \Phi + r_{Kb}^s \cos \Phi), \quad \Phi(t_0) = \Phi_0 \quad (10)$$

$$\dot{\Theta} = q_{Kb}^s \cos \Theta - r_{Kb}^s \sin \Phi, \quad \Theta(t_0) = \Theta_0 \quad (11)$$

$$\dot{\Psi} = \frac{q_{Kb}^s \sin \Phi + r_{Kb}^s \cos \Phi}{\cos \Theta}, \quad \Psi(t_0) = \Psi_0 \quad (12)$$

The integration of the kinematic equations requires initial values for the velocity ( $u_0, v_0, w_0$ ), the position ( $x_{g,0}, y_{g,0}, h_{g,0}$ ) and the aircraft attitude ( $\Phi_0, \Theta_0, \Psi_0$ ) at the beginning of the considered maneuver time slice  $t_0$ . These initial states are determined during the parameter estimation process. Note that the kinematic equations do not depend on the mass properties of the aircraft. Therefore, the FPR method can be applied independently of the aircraft mass and CG position as the method relies only on the geometric positions of the sensors.

### 3.3 Aerodynamic Flow Conditions

The aerodynamic velocity components calculated with Eqs. 1 to 9 are local velocities determined at the position of the inertial reference platform. For each model of the air data sensors, these velocities have to be transformed to local velocities at the position of the dedicated air data sensor. These can be determined from the



position coordinates of the IRS and the air data sensor, and the measured angular rates:

$$u_{ADS}^l = u_{Ab} - (y_{ADS} - y_{IRS}) \cdot r_{Kb}^s + (z_{ADS} - z_{IRS}) \cdot q_{Kb}^s \quad (13)$$

$$v_{ADS}^l = v_{Ab} + (x_{ADS} - x_{IRS}) \cdot r_{Kb}^s - (z_{ADS} - z_{IRS}) \cdot p_{Kb}^s \quad (14)$$

$$w_{ADS}^l = w_{Ab} - (x_{ADS} - x_{IRS}) \cdot q_{Kb}^s + (y_{ADS} - y_{IRS}) \cdot p_{Kb}^s \quad (15)$$

Note that the air data sensors for the different systems (ADS1 and ADS2) have different positions on the aircraft (see also Fig. 2). With the local velocity components, the local  $V_{TASADS}^l$ , angle of attack  $\alpha_{ADS}^l$  and angle of sideslip  $\beta_{ADS}^l$  at the air data sensor position can be obtained:

$$V_{TASADS}^l = \sqrt{(u_{ADS}^l)^2 + (v_{ADS}^l)^2 + (w_{ADS}^l)^2} \quad (16)$$

$$\alpha_{ADS}^l = \arctan\left(\frac{w_{ADS}^l}{u_{ADS}^l}\right) \quad (17)$$

$$\beta_{ADS}^l = \arcsin\left(\frac{v_{ADS}^l}{V_{TASADS}^l}\right) \quad (18)$$

The local flow velocities and angles are used as input values for the sensor model as described in the FPR procedure in section 3.1.

The basic air data systems provide also other quantities like static and total pressure, total and static air temperature, barometric altitude, Mach number and  $V_{CAS}$ . For these air data parameters local reference values have to be determined as well to setup sensor models for these quantities. Since the nose boom pressure and temperature sensors were calibrated and tested prior to the flight test campaign, it was assumed that these sensors would provide the best air data measurements. The static pressure  $p_{statNB}^s$  and temperature  $T_{statNB}^s$  measurements from the nose boom were therefore used as input to the FPR model to determine the atmospheric conditions used as reference for the basic air data systems ADS1 and ADS2. These two air data parameters were used as local static pressure and temperature reference of the basic avionic air data systems:

$$p_{statADS}^l = p_{statNB}^s \quad (19)$$

$$T_{statADS}^l = T_{statNB}^s \quad (20)$$

The local barometric altitude  $h_{baroADS}^l$  is determined from the static pressure  $p_{statNB}^s$  using the following equation:

$$h_{baroADS}^l = \frac{T_N}{\gamma_H} \left( 1 - \left( \frac{p_{statNB}^s}{p_n} \right)^{\frac{1}{5.255}} \right) \quad (21)$$

The local reconstructed  $V_{TASADS}^l$  determined with Eq. 16 is used to calculate the local reference Mach number  $Ma_{ADS}^l$  is determined from the static air temperature  $T_{statNB}^s$ :

$$Ma_{ADS}^l = \frac{V_{TASADS}^l}{\sqrt{T_{statNB}^s \cdot \kappa \cdot R}} \quad (22)$$

Having determined the Mach number, the total air temperature and the total pressure is calculated with the following equations:

$$T_{totADS}^l = T_{statNB}^s \left( 1 + 0.2 (Ma_{ADS}^s)^2 \right) \quad (23)$$

$$p_{totADS}^l = p_{statNB}^s \left( 1 + 0.2 (Ma_{ADS}^s)^2 \right)^{3.5} \quad (24)$$

Finally, the computed airspeed is determined from the difference between total and static pressure:

$$V_{CASADS}^l = a_n \cdot \sqrt{5 \left( \left( \frac{p_{totADS}^l - p_{statNB}^s}{p_n} + 1 \right)^{\frac{2}{\gamma}} - 1 \right)} \quad (25)$$

### 3.4 Parameter Estimation Setup

The quality of the reconstructed air data signals depends directly on the accuracy of the inertial measurements provided by the IRS. As there were four different IRS platforms available on the ISTAR, for each platform the measured accelerations and angular rates were evaluated during the DCC process. IRS3 was selected as input for the FPR process, because it provided the signals with the best quality. The final selection of input signals for the FPR process is presented in Tab. 1.

**Table 1 Selected input signals for the FPR.**

No.	Variable	Description
1	$a_{xKbIRS3}^s$	Body longitudinal acceleration IRS3.
2	$a_{yKbIRS3}^s$	Body lateral acceleration IRS3.
3	$a_{zKbIRS3}^s$	Body vertical acceleration IRS3.
4	$p_{KbIRS3}^s$	Roll rate IRS3.
5	$q_{KbIRS3}^s$	Pitch rate IRS3.
6	$r_{KbIRS3}^s$	Yaw rate IRS3.
7	$p_{statNB}^s$	Nose boom static pressure.
8	$T_{statNB}^s$	Nose boom static air temperature.

As mentioned in section 3.1, the output error estimation algorithm compares the modeled sensor output with the measured sensor signals. The signals selected for the output comparison are also called weighted signals. For a the identification of a specified sensor model it is necessary to weight the corresponding signal in the output and select the model parameters for the estimation process. The Maximum Likelihood algorithm is an iterative process. The more estimation parameters and weighted signals are selected, the higher the computational complexity. At the beginning of the FPR usually only a few signals are weighted with simple model parameters to determine a first set of initial values for the states in Eqs. 1 to 12. In this case for example, one would only select  $V_{TASNB}$ ,  $\alpha_{NB}$ ,  $\beta_{NB}$ ,  $\Phi_{IRS3}$ ,  $\Theta_{IRS3}$ ,  $\Psi_{IRS3}$  as weighted signals on the output and no sensor parameter for estimation. During the data compatibility analysis of the ISTAR flight test data, the complexity of the sensor models was extended in several steps. In order to find the best fit for a sensor model, the number of parameters is increased with each step. This concerns also the number of weighted signals in the output. The final set of weighted signals used for the FPR process is presented in Tab. 2. The geodetic positions and velocities given in the table rows number three and four are weighted for the estimation of the horizontal wind components as explained in section 3.2. For the position coordinates, the signals from the additional IRS were weighted, because concerning these signals it provided a better measurement quality. This could be caused by a better GPS receiver system which is using a more recent correction setup than the basic avionic.

## 4 Examples and Results

In the following section selected examples from the current ISTAR system identification flight test campaign are presented. It should be mentioned that the described process was repeated with flight data containing aircraft configurations with extended flaps and extended landing gear. Since the aircraft configuration has an influence on the fuselage flow field, slightly different sensor model parameters were estimated for these cases.

**Table 2 Weighted signals at the FPR model output.**

No.	Variable	Description
1	$\Phi_{IRS3}, \Theta_{IRS3}, \Psi_{IRS3}$	Body roll, pitch and yaw angle IRS3.
2	$V_{NKgIRS3}, V_{EKgIRS3}, V_{DKgIRS3}$	Inertial velocities in north, east and down direction IRS3.
3	$Lat_{IRS}, Lon_{IRS}$	Latitude and longitude position additional IRS.
4	$Alt_{IRS}$	Inertial WGS84 altitude additional IRS.
5	$p_{statADS1}, p_{statADS2}, p_{statNB}$	Static pressure ADS1, ADS2 and nose boom.
6	$p_{totADS1}, p_{totADS2}, p_{totNB}$	Total pressure ADS1, ADS2 and nose boom.
7	$T_{statADS1}, T_{statADS2}, T_{statNB}$	Static air temperature ADS1, ADS2 and nose boom.
8	$T_{totADS1}, T_{totADS2}, T_{totNB}$	Total air temperature ADS1, ADS2 and nose Boom.
9	$h_{pADS1}, h_{pADS2}, h_{pNB}$	Pressure altitude ADS1, ADS2 and nose boom.
10	$Ma_{ADS1}, Ma_{ADS2}, Ma_{NB}$	Mach No. ADS1, ADS2 and nose boom.
11	$V_{CASADS1}, V_{CASADS2}, V_{CASNB}$	Calibrated airspeed ADS1, ADS2 and nose boom.
12	$V_{TASADS1}, V_{TASADS2}, V_{TASNB}$	True airspeed ADS1, ADS2 and nose boom.
13	$AOALHADS, AOARHADS$	Basic avionic indicated left hand / right hand angle of attack.
14	$AOANB, AOSNB$	Nose boom indicated angle of attack, indicated angle of sideslip.

#### 4.1 Calibration of Angle of Attack and Angle of Sideslip Nose Boom Vanes

One of the first actions after the flight tests for the aerodynamic system identification was the verification and correction of the nose boom measurement data. A total of 304 maneuver data segments were evaluated for the clean aircraft configuration. The results for the nose boom  $\alpha$  and  $\beta$  wind vane sensors are shown in Fig. 6, where the model output and the sensor measurement are plotted against the local reference ( $\alpha_{NB}^l, \beta_{NB}^l$ ), calculated from the reconstructed velocity components. Ideally, the model should represent the measured output and the two plots should be superimposed. Figures 6a and 6b show the results without any estimated model parameters. The absence of large offsets between measured and modeled values indicates that the existing calibration of the sensors is already of good quality. However, for angle of attack values greater than  $4^\circ$  and sideslip angles less than  $0^\circ$ , a significant mismatch between model and measurement is visible. The FPR results with estimated model parameters are shown in Fig. 6c and Fig. 6d. Compared to the plots with the uncorrected model, the differences are significantly minimized. The sensor model for the  $\alpha$ -vane sensors are represented by the following equations:

$$\alpha_{NB}^m = \alpha_{NB}^l(t - \tau_{AOANB}) \cdot (1 + f_{AOANB}) + f_{AOANB\beta} \cdot \beta_{NB}^s + b_{AOANB} \quad (26)$$

A similar model approach was formulated for the  $\beta$  nose boom wind vane:

$$\beta_{NB}^m = \beta_{NB}^l(t - \tau_{AOSNB}) \cdot (1 + f_{AOSNB}) + f_{AOSNB\alpha} \cdot \alpha_{NB}^s \quad (27)$$

The estimated model parameters are listed in Table 3 together with their standard deviation.

**Table 3 FPR model parameters for the nose boom wind vanes sensors.**

Parameter	Unit	Value	$\sigma_s$	Parameter	Unit	Value	$\sigma_s$
$b_{AOANB}$	rad	-0.0072	$1.2678 \cdot 10^{-05}$	$f_{AOSNB}$	-	0.0727	$4.2246 \cdot 10^{-04}$
$f_{AOANB}$	-	0.0810	$1.6820 \cdot 10^{-04}$	$f_{AOSNB\alpha}$	-	-0.0341	$2.8284 \cdot 10^{-04}$
$f_{AOANB\beta}$	-	0.0236	$1.9262 \cdot 10^{-04}$	$\tau_{AOSNB}$	s	0.0734	$4.2485 \cdot 10^{-04}$
$\tau_{AOANB}$	s	0.0755	$4.1083 \cdot 10^{-04}$				

A systematic step-by-step approach was used to find a model structure in Eqs. 26 and 27 which is reducing the error between the model and the measurement. Besides bias and factor parameters other influence quantities like  $\alpha$  and  $\beta$  factors were evaluated and an appropriate term was added to the equations. Compressibility on the vane measurements was also evaluated, but no significant influence was found. This may change if more flight data with higher Mach numbers becomes available to the FPR process. The impact of the estimated model parameters on the remaining error between model and measurement are depicted in Fig. 7 and Fig. 8. The remaining model errors of the wind vanes sensors ( $\Delta\alpha_{NB}$ ,  $\Delta\beta_{NB}$ ) are plotted against the local reference angle of attack and angle of sideslip ( $\alpha_{NB}^l$ ,  $\beta_{NB}^l$ ). Data from all maneuvers for the uncorrected model with no estimated parameters are shown in red together with a linear regression as a black dashed line. The blue lines show the data for the corrected model with estimated parameters. The black line shows the respective linear regression over all data for the corrected model. Bias and factor of the regression lines are shown in the plot legends. For both wind vanes the errors could be reduced significantly and are in a range of  $\pm 0.5^\circ$ .

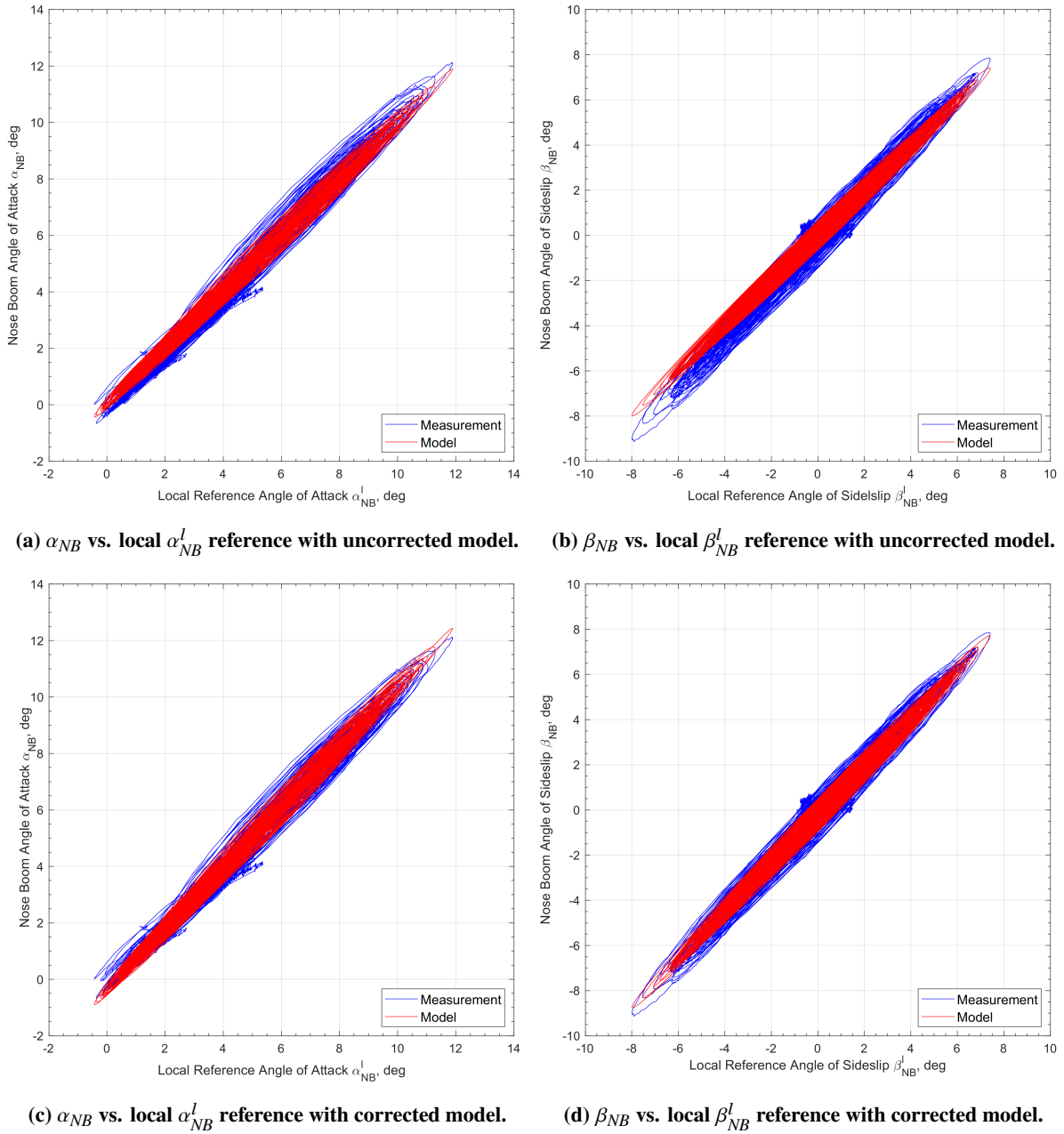


**Fig. 6 Comparison of nose boom wind vane sensor models output and measurements.**

The coefficients of the regression line indicate also that for both sensors the linear error trend could be nearly removed. The identified sensor models for the wind vanes were applied for the correction of the nose boom

measurements. For this purpose the Eq. 26 was inverted using the sensor measurements as input for the calculation of  $\alpha_{NB}^l$  and  $\beta_{NB}^l$ . The calibrated nose boom data was used as a reference for other sensors which is discussed in the following section.

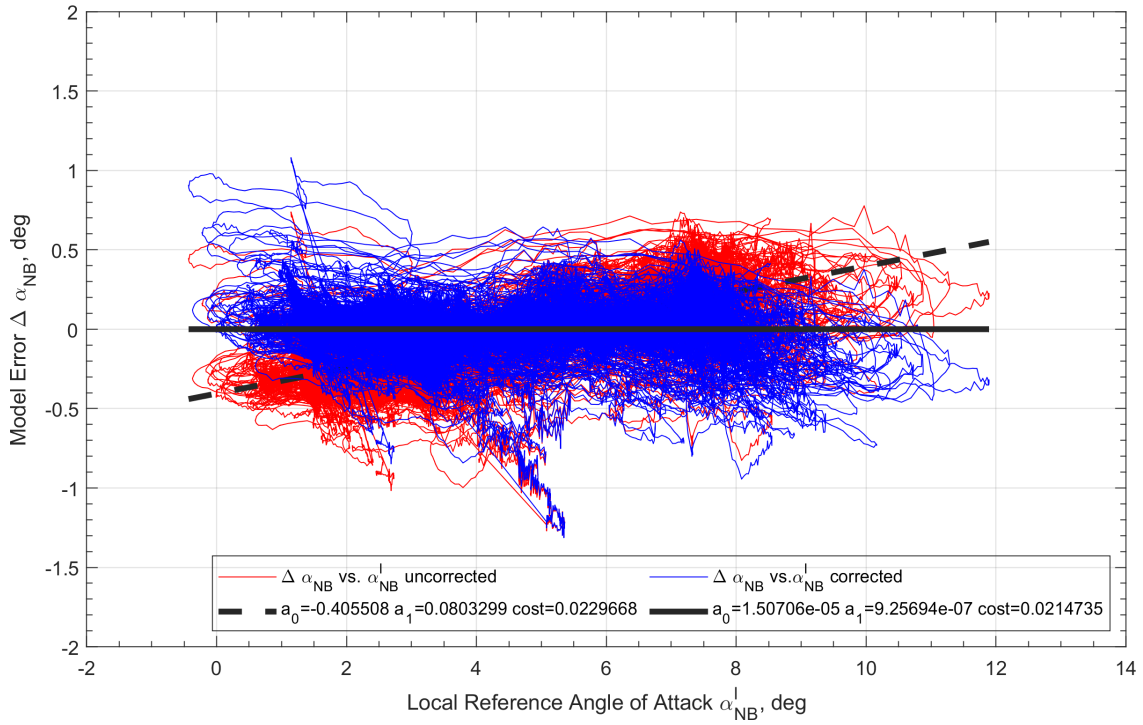


**Fig. 7 Remaining angle of attack model error vs. local reference  $\alpha_{NB}^l$ .**

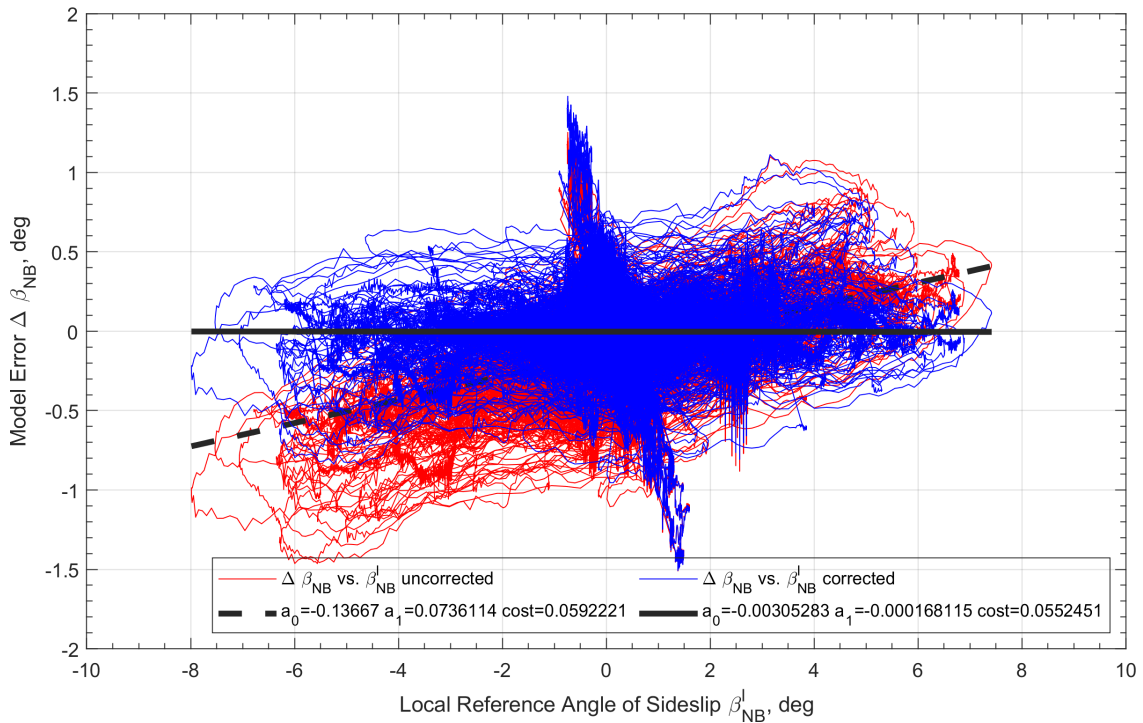


**Fig. 8 Remaining angle of sideslip model error vs. local reference  $\beta_{NB}^l$ .**

## 4.2 Checking of the Basic Avionic Angle of Attack Vane Calibration

In this case, the characteristics of the measured air data signals must be known before they can be used as input for control applications. In this section, the measurement characteristics of the basic avionic left hand angle of attack

vane are analyzed and corrected using the FPR method. The readings from the basic avionic  $\alpha$ -vanes were provided on the aircraft data bus as indicated angle of attack signals without corrections. To calculate the true  $\alpha$  from the indicated angle of attack measurements, the aircraft manufacturer provided a calibration function with parameters. During the DCC, this original calibration of the left hand  $\alpha$ -vane was compared to a new calibration function, resulting from an identified sensor model with the FPR process.

The true angle of attack was calculated from the left hand angle of attack vane measurements using the original calibration function and the identified one, taking into account all flight maneuvers for the clean aircraft configuration. Figure 9 shows a comparison between these two different calibration setups for the basic avionic vane and the corrected nose boom  $\alpha$ -vane measurement. The linear regression functions for the true angle of attack are plotted against the local angle of attack reference. The bias and factor of the regression functions are again shown in the plot legend. The red line is the regression line for the original calibration function and shows an offset from the diagonal, indicating a measurement error. The regression lines of the nose boom (dashed black) and the  $\alpha$  calculated with the calibration function determined by FPR (blue) lie on top of each other, almost on the plot diagonal. This indicates that the new calibration has significantly reduced the measurement error. Analysis of the flight data showed that the main error in the left hand  $\alpha$ -vane is due to flow effects during large sideslip maneuvers. This phenomenon is illustrated in Fig. 10, where the difference between the true nose boom angle of attack and the basic avionic left hand  $\alpha$ -vane ( $\Delta\alpha_{NB,LH}$ ) is plotted against the local nose boom angle of sideslip ( $\beta_{NB}^s$ ) reference.

The red lines represent the flight data with the original factory calibration, the blue lines the new calibration based on the FPR method. The black dashed and solid lines show the corresponding linear regression function. The true left hand  $\alpha$  determined with the original calibration function shows a clear dependence on the sideslip. The difference from the calibrated nose boom angle of attack reaches nearly  $0.8^\circ$  when the sideslip angle has a value of  $8^\circ$ . The sensor model identified with the FPR process is similar to the nose boom sensor model defined by Eq. 26. An angle of sideslip dependency factor is part of the model equations. Table 4 lists the estimated parameters for the left hand  $\alpha$ -vane sensor model.

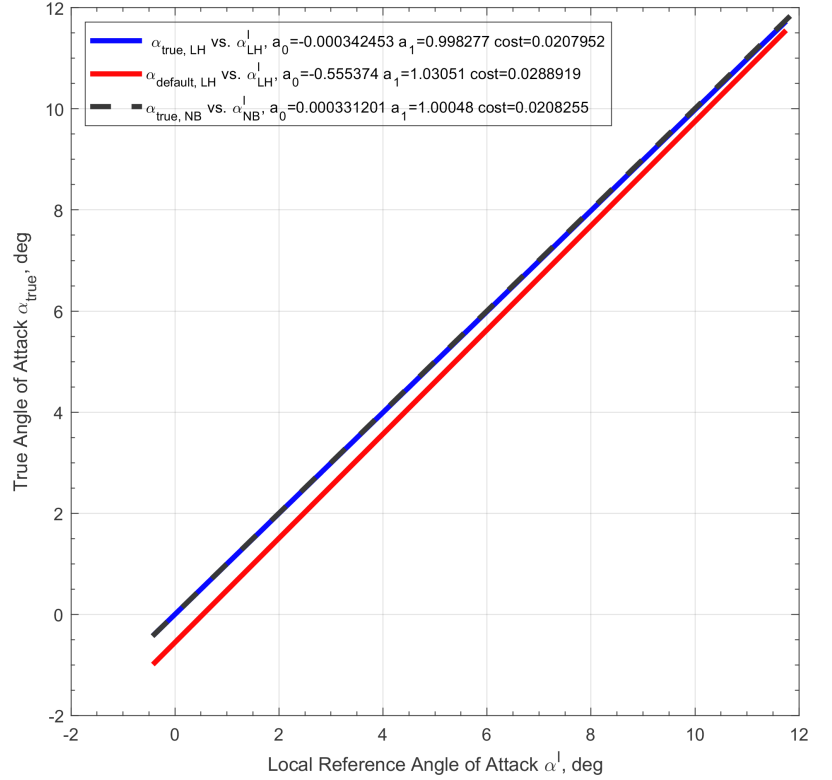


**Fig. 9 Results for the linear regression of the true  $\alpha$  measurements from the nose boom (dashed black), the left hand basic avionic  $\alpha$ -vane with original manufactures calibration parameters (red) and parameters estimated with the FPR process (blue) plotted against the local angle of attack reference.**

**Table 4 FPR Model Parameters for the LH basic avionic wind vanes sensor.**

Parameter	Unit	Value	$\sigma_s$
$b_{AOALH}$	rad	0.0178	$2.2917 \cdot 10^{-05}$
$f_{AOALH}$	-	0.9063	$3.0473 \cdot 10^{-04}$
$f_{AOALH,\beta}$	-	-0.0918	$3.4766 \cdot 10^{-04}$
$\tau_{AOALH}$	s	0.0640	$4.3161 \cdot 10^{-04}$

With the identified model, the sideslip dependence in the measurement error could be nearly reduced, as indicated by the black solid regression line in Fig. 10. The remaining total to the calibrated true nose boom  $\alpha$  is between  $-0.4^\circ$  and  $+0.2^\circ$ . This example demonstrates how the FPR can be used to check the validity of basic avionic flight data during non-standard operational maneuvers that may occur during the use of the ISTAR as a research aircraft. Similar analysis and corrections were also performed on the right hand  $\alpha$ -vane of the basic avionic air data system.

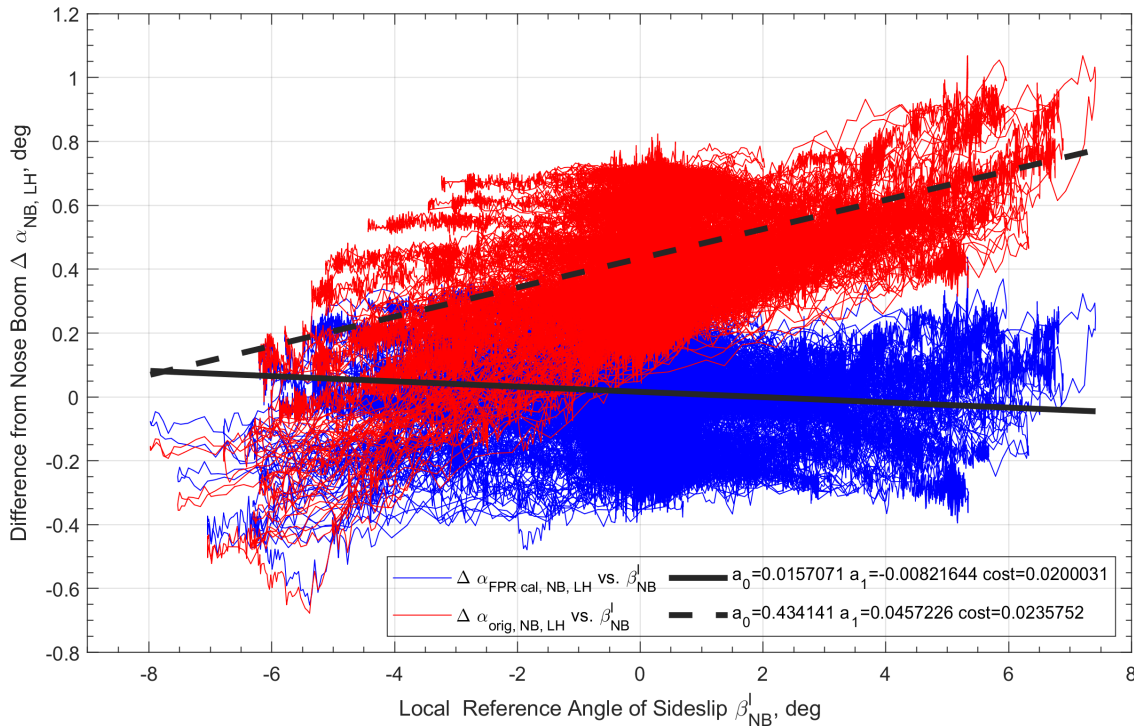


**Fig. 10** Difference between the true nose boom  $\alpha$  and the true  $\alpha$  of the left hand basic avionic vane vs. the local nose boom sideslip reference. In red using the original manufactures calibration, in blue using the new calibration parameters from the FPR results.

### 4.3 Pressure Measurements During Sideslip Maneuvers

Asymmetric flow conditions, such as those encountered during large sideslip maneuvers, can affect pressure sensor readings with the current ISTAR configuration, i.e. the nose boom attached, which presumably cause a disturbance of the flow for large side slip angles. During normal aircraft operation, such situations may occur during landing and takeoff under strong side winds. Under high sideslip conditions, one side of the fuselage is in the wind shadow while the other side experiences a direct inflow. This effect on the total pressure sensor is shown in Fig. 11, where the difference between the nose boom and the uncorrected ADS1 total pressure is plotted against the nose boom angle of sideslip in blue lines. The nose boom total and static pressure measurements are used as a reference in this case, because they are calibrated and measure the pressures in front of the aircraft. A DCC analysis of the nose boom pressure measurements was performed prior to this analysis and shows that the nose boom calibration almost compensates for sideslip effects. The ADS1 total pressure, however is installed on the left hand side of the cockpit as shown in Fig. 2. In case of a positive  $\beta$ , the sensor is shadowed by the nose of the aircraft, resulting in a difference of more than 11 mbar to the nose boom reading as shown in Fig. 11. However, as the graph shows, there are maneuvers with a positive  $\alpha$ , where the difference remains at 2 mbar, which is in the same range as maneuvers with a negative  $\beta$ . Further analysis of this characteristic shows that the large differences occur only for maneuvers where the angle of attack is less than  $3.8^\circ$ . Flight data measurements with a positive  $\beta$  and an  $\alpha$  equal to and below  $3.8^\circ$  are marked with red dots in the plot. Geometrical considerations have led to the conclusion that the described effect could be caused by the nose boom. The positions of the total pressure probes as presented in Fig. 2 indicate that they could possibly be in the wake of the nose boom installation. To correct for this "shadowing" effect, a model had to be found in the FPR process.

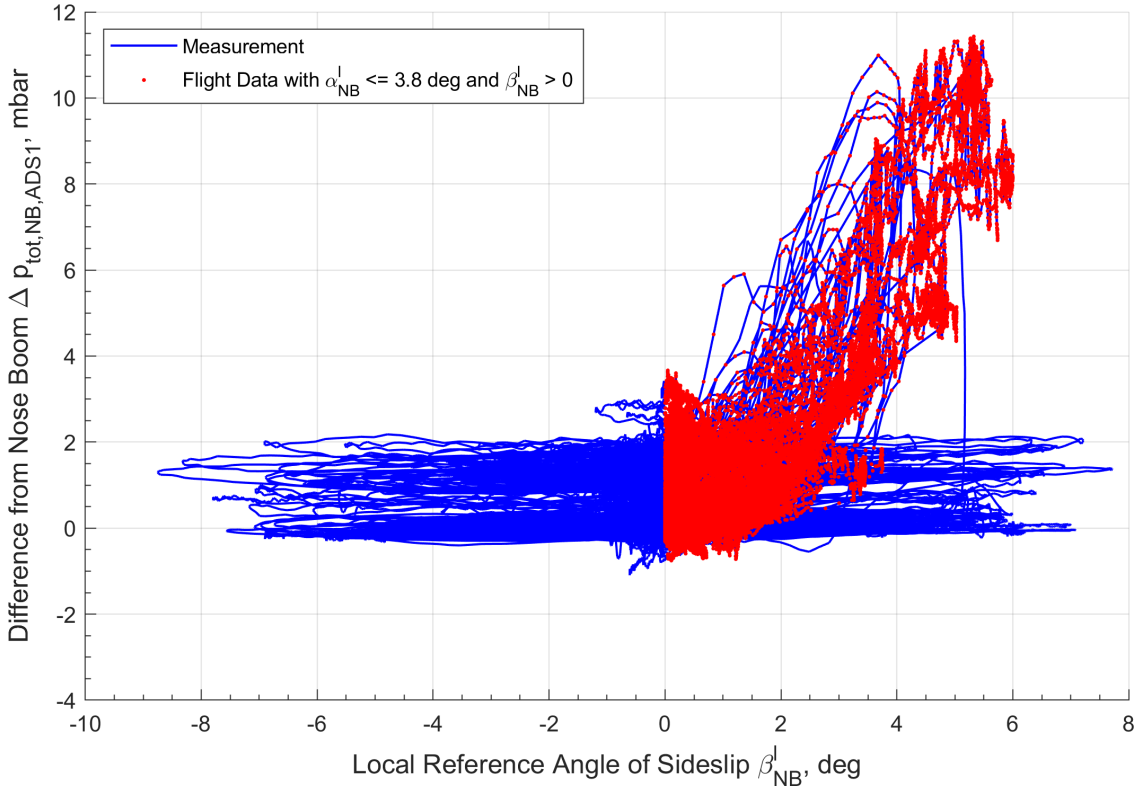


**Fig. 11** Difference between nose boom and uncorrected ADS1 total pressure vs. nose boom angle of sideslip.

An approach for a sensor model of the total pressure measured by the ADS1 is presented in the following equation:

$$p_{tot\ ADS1}^m = p_{tot\ ADS1}^l(t - \tau_{p\ tot\ ADS1}) + b_{p\ tot\ \beta\ ADS1} + b_{p\ tot\ ADS1} \quad (28)$$

$$b_{p\ tot\ \beta\ ADS1} = \begin{cases} 0 & \text{if } \beta_{NB}^l \leq 0 \\ 0 & \text{if } \beta_{NB}^l > 0 \wedge \alpha_{NB}^l > 3.8^\circ \\ f_{p\ tot\ \beta\ ADS1} \cdot \beta_{NB}^l & \text{if } \beta_{NB}^l > 0 \wedge \alpha_{NB}^l \leq 3.8^\circ \end{cases}$$

This nonlinear model approach introduces a  $\beta$ -dependent term that is only considered when the sideslip angle is positive and the angle of attack is less than  $3.8^\circ$ . Using the identified sensor model parameters listed in Tab. 5, a correction was applied to the ADS1 total pressure measurements. The result of this correction is shown in Fig. 12, where the difference of the corrected ADS1 measurements to the nose boom total pressure is plotted against  $\beta$ . Compared to the uncorrected measurements in Fig. 11, the difference could be reduced to a value below 6 mbar for most of the sideslip maneuvers. The correction of the ADS1 total pressure resulted in a better agreement with the nose boom measurements. However, the diagram in Fig. 12 shows that for some maneuvers there is an overcompensation of the sideslip influence. This is indicated by the flight data measurements, which show a difference towards -2 mbar on the side with a positive  $\beta$ . Further analysis with more flight data, including maneuvers with larger sideslip angles, is needed to identify a better model for the sensor correction. With additional data it should be possible to find a more adequate sensor model. Although the ADS1 static pressure ports on both sides of the fuselage are connected by pressure tubes, the DCC analysis also showed a  $\beta$ -dependence on the static pressure measurements. A sensor model for the static pressure measurements was identified using the following equation:

$$p_{stat\ ADS1}^m = p_{stat\ ADS1}^l + f_{p\ stat\ \beta\ ADS1} \cdot \beta_{NB}^l + b_{p\ stat\ ADS1} \quad (29)$$

Table 5 contains the estimated sensor parameters resulting from the FPR process. In the same manner sensor models were identified for ADS2 which showed nearly the same  $\beta$ -dependencies for the total pressure, in this case towards the side with a negative  $\beta$ .



The computed airspeed  $V_{CAS}$  is calculated from the difference between total and static pressure according to Eq. 25. Deviations in the measured pressures at large sideslip angles therefore have a direct effect on the calculated airspeed. These effects can be observed particularly well during sideslip maneuvers at constant heading, as shown in Fig. 13. Here, the flight data measurements are shown for two different steady heading sideslip maneuvers, one with a positive and one with a negative  $\beta$ .

**Table 5 FPR Model Parameters for the ADS1 pressure sensors.**

Parameter	Unit	Value	$\sigma_s$
$b_{p\ stat\ ADS1}$	Pa	-39.44	$7.3538 \cdot 10^{-02}$
$f_{p\ stat\ \beta\ ADS1}$	Pa/rad	-1097.28	$2.1925 \cdot 10^{+00}$
$b_{p\ tot\ ADS1}$	Pa	17.67	$1.6263 \cdot 10^{-01}$
$f_{p\ tot\ \beta\ ADS1}$	Pa/rad	-6336.25	$1.0693 \cdot 10^{+01}$
$\tau_{p\ tot\ ADS1}$	s	0.2837	$1.2410 \cdot 10^{-03}$

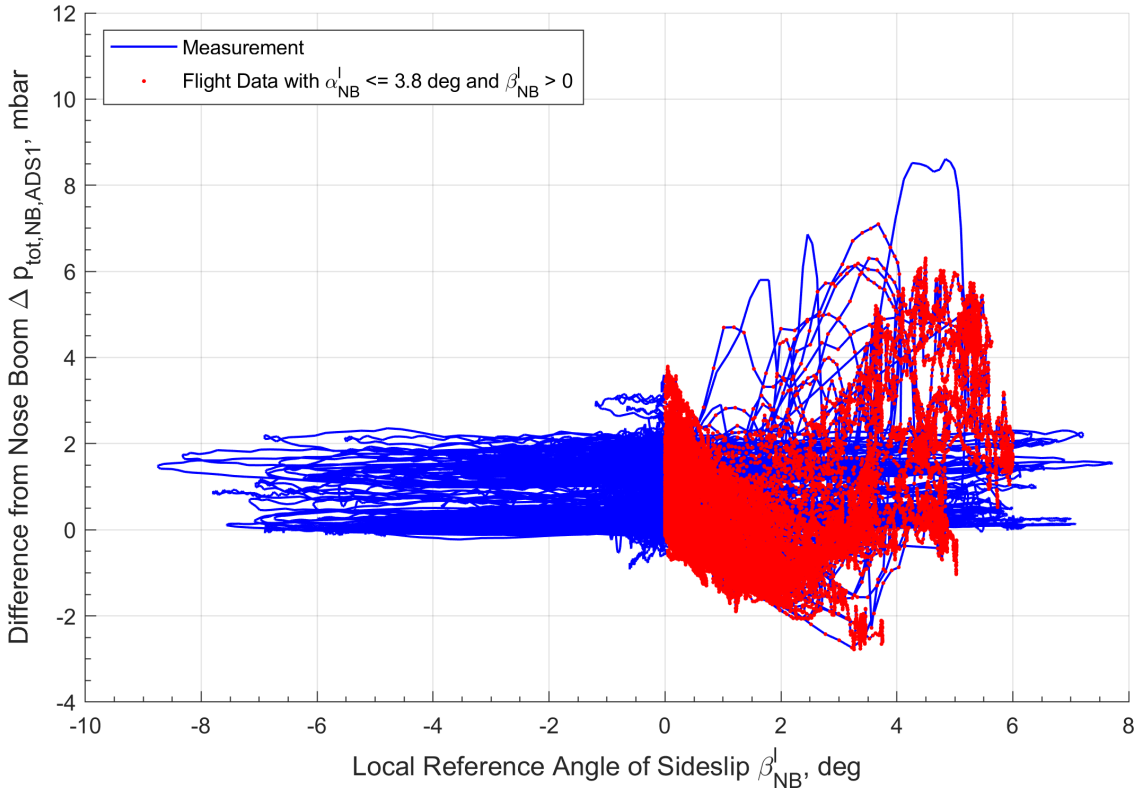


**Fig. 12 Difference between nose boom and uncorrected ADS1 total pressure vs. nose boom angle of sideslip.**

The first graph shows plots for the angle of attack and angle of sideslip measured by the nose boom. The other plots show the static pressure, total pressure and computed airspeed from the nose boom sensor, the uncorrected and the corrected ADS1 sensor readings. For both maneuvers the angle of attack is around  $2.5^\circ$  and well below  $3.8^\circ$ . The first maneuver shows that as the sideslip increases, the uncorrected ADS measurements begin to deviate from the nose boom readings. The corrected signals still have an offset to the nose boom measurements, but it is much smaller. At the maximum  $\beta$  of nearly  $6^\circ$ , the resulting  $V_{CAS}$  from ADS1 deviates from the nose boom by more than 8 kts, while the  $V_{CAS}$  determined with the corrected quantities shows an offset of only 3 kts. For the second maneuver with a negative  $\beta$ , the deviations of the uncorrected ADS1 measurements are much smaller and only visible in the static pressure and the resulting  $V_{CAS}$ . In this case, the ADS1 total pressure sensor is less affected by shadowing effects. The corrected values for the ADS1 static pressure and  $V_{CAS}$  are nearly equal to the signals from the nose boom measurements. In general, the corrections found with the FPR method improved the ADS1 static and total pressure measurements. This example shows that the DCC method can be effectively

applied to analyze and correct various sensor characteristics. Although the identified sensor model is not able to correct all asymmetric flow effects, the DCC allows to evaluate the deviations from reference quantities such as the nose boom measurements and the reconstructed velocity components. The influence of the boom installation on the basic avionic pressure sensors must be further analyzed with data from flights with and without installed nose boom.

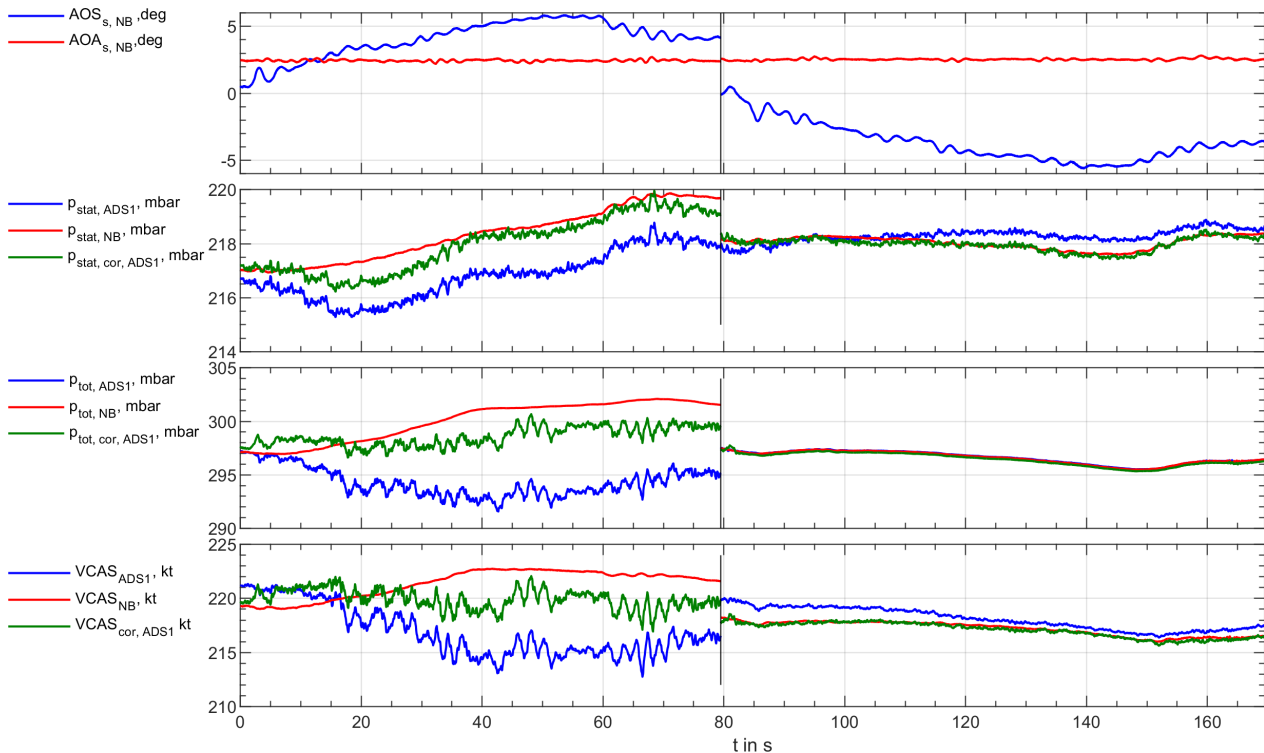


**Fig. 13** Flight data from two steady heading sideslip maneuvers with nose boom measurements as reference (red), uncorrected (blue) and FPR corrected measurements (green) from ADS1.

## 5 Conclusion and Outlook

In this paper an introduction to the data compatibility check method was given and its advantages for the evaluation of flight data measurements were discussed. The flight path reconstruction process was presented as a method to reconstruct flight data quantities from measured inertial accelerations and angular rates. Examples from the current system identification flight test campaign for the new DLR research aircraft ISTAR were presented with the setup used for the analysis of flight test sensor measurements. Data from the nose boom angle of attack and angle of sideslip measurements were verified and sensor models for calibration were identified. The FPR process was also applied to basic avionic systems such as the ADS1 sensors for angle of attack, static and total pressure. Correction functions for these sensor measurements were identified for large sideslip angle maneuvers, causing asymmetric flow conditions.

The results of the DCC will be used for the next steps in the qualification of ISTAR as a variable stability system research aircraft. These include the identification of a nonlinear aerodynamic model and the selection and conditioning of sensor measurements to be used for flight control applications. Sideslip angle information will not be available in cases where operating conditions do not permit the installation of a nose boom. Therefore, the results of the DCC analysis will be used to create a synthetic angle of sideslip based on a sensor model using lateral acceleration, yaw rate, and rudder deflection as input values.

An additional test program with the ISTAR is planned to complete the flight database with maneuvers performed at higher speeds. The collected data will be used to improve the sensor models identified with the FPR process. This concerns also further research on compressibility effects at high Mach numbers. A detailed analysis will also be performed on the effects of the nose boom installation on the basic avionic air data sensors.

## Acknowledgments

The results presented in this paper are part of the DLR internal project HighFly (High speed inflight validation). I would like to thank my colleagues working at the Department of Flight Test Instrumentation at the DLR Institute of Flight Systems for their help with FTI equipment and electrical installations and the people at the DLR Flight Experiments division for flight operations and certification issues.

## References

- [1] V.Klein and J. R. Scheiss. Compatibility check of measured aircraft responses using kinematic equations and extended kalman filter. *NASA TN D-8514*, 1977.
- [2] J.A. Mulder, Q.P. Chu, J.K. Sridhar, J.H. Breeman, and M. Laban. Non-linear aircraft flight path reconstruction review and new advances. *Progress in Aerospace Sciences*, 35(7):673 – 726, 1999. Cited by: 80. DOI: [10.1016/S0376-0421\(99\)00005-6](https://doi.org/10.1016/S0376-0421(99)00005-6).
- [3] D. A. Keskar and V. Klein. Determination of instrumentation errors from measured data using maximum likelihood method. *AIAA Paper 80-1602*, 1980.
- [4] R. V. Jategaonkar. *Flight vehicle system identification*. American Institute of Aeronautics and Astronautics, Reston, jan 2015. ISBN: 978-1-56347-836-9. DOI: [10.2514/4.866852](https://doi.org/10.2514/4.866852).
- [5] Andreas Giez, Christian Mallaun, Vladyslav Nenakhov, and Martin Zöger. Calibration of a nose boom mounted airflow sensor on an atmospheric research aircraft by inflight maneuvers. Technical report, URL: <https://elib.dlr.de/145969/>, November 2021.
- [6] Andreas Giez, Martin Zöger, Volker Dreiling, and Christian Mallaun. Static source error calibration of a nose boom mounted air data system on an atmospheric research aircraft using the trailing cone method. Technical report, URL: <https://elib.dlr.de/145770/>, 2020.
- [7] D. Niedermeier, K. Giese, and D. Leißling. The new research aircraft ISTAR - experimental flight control system. *33rd Congress of the International Council of the Aeronautical Sciences*, 4. - 9. September 2022, Stockholm, (0439), 2022.
- [8] Dassault Aviation. Falcon 2000LX aircraft maintenance manual (AMM). 2022.
- [9] M. Gestwa, D. Leißling, C. Pätzold, and C. Raab. The new DLR-research aircraft ISTAR - past, present and future. *Symposium of the Society of Flight Test Engineers*, 10. - 11. Mai 2022, Nürnberg, 2022.
- [10] S. Seher-Weiss. Fitlabgui - a versatile tool for data analysis, system identification and helicopter handling qualities analysis. *42nd European Rotorcraft Forum 2016*, 2:1503–1521, 2016.